Relationship between the migration of crustal material, normal faulting, and gneiss domes in the vicinity of the Dinggye region, central part of the Tethys–Himalaya terrane
Insights from the 3-D electrical structure

Sheng, Yue; Jin, Sheng; Comeau, Matthew J.; Hou, Zengqian; Zhang, Letian; Wei, Wenbo; Ye, Gaofeng

Important note
To cite this publication, please use the final published version (if applicable).
Please check the document version above.

Relationship between the migration of crustal material, normal faulting, and gneiss domes in the vicinity of the Dinggye region, central part of the Tethys–Himalaya terrane: Insights from the 3-D electrical structure

Yue Sheng [a], Sheng Jin [a,b,*], Matthew J. Comeau [c], Zengqian Hou [d,**], Letian Zhang [a,b], Wenbo Wei [a,b], Gaofeng Ye [a,b]

[a] *School of Geophysics and Information Technology, China University of Geosciences, Beijing 100083, China*
[b] *Key Laboratory of Geo-detection of Ministry of Education, Beijing 100083, China*
[c] *Department of Geoscience and Engineering, Delft University of Technology, 2628 CN, Delft, The Netherlands*
[d] *Key Lab of Continental Tectonics and Dynamics, Institute of Geology, Chinese Academy of Geological Sciences, Beijing 100037, China*

ARTICLE INFO

ABSTRACT

The Dinggye region, in the central part of the Himalayan orogenic belt, includes the southern part of the Xainza-Dinggye rift and the Mabja Gneiss Dome with leucogranite cores. Previous studies of gneiss domes in this region report the existence of channel flow processes or tectonic exhumation, in addition to partial melting of orogenic mid-crust. However, the relationship between the crustal migration of materials and the north-south-trending normal rifts remains largely unexplored. In this work, we generate a new 3-D electrical resistivity model from an array of magnetotelluric data in the Dinggye region and examine it in addition to other electrical resistivity models to the north and east from previous works. By comparing the geophysical models with available geological and geochemical evidence, we find a clear relationship between the electrical resistivity structure, the presence of gneiss domes, north-south-trending normal rifting, and deep plunging subduction which is related to the source of Helium isotopes (crustal or mantle origin). Overall, the results suggest that the southern migration of lithospheric materials likely contributed to the evolution of the rifts in the Tethys-Himalaya terrane, which also may have been influenced by uplifting and cooling of gneiss domes. The models are consistent with tearing of the Indian lithosphere beneath the Xainza-Dinggye rift and other adjacent rifts. Additionally, the difference in the electrical structure related to the Indian crust along the east-west direction likely results from the exhumation of the continental slab, metamorphism in the Tethys-Himalaya terrane, and southern extrusion of materials in the Lhasa terrane.

1. Introduction

The Himalayan orogenic belt is the product of the collision of the Indian and Eurasian continental plates, a type example of orogenic belts worldwide, and a natural laboratory used for building theories of orogeny and models of tectonic evolution (Yin and Harrison, 2000). Since the Cenozoic, this belt has experienced high and ultrahigh pressure metamorphism, rapid exhumation of deep crustal material and subsequent decompression, partial melting, and anatexis of the Himalayan deep crust (e.g., Lee et al., 2006; Lin et al., 2020). The Tethys-Himalaya terrane in the north of the Himalayan orogenic belt is

characterized by pervasive extensional structures such as N–S-trending normal rifts and the North Himalayan Gneiss Dome (NHGD). Two different types of domes are reported in the NHGD, the core of which consists of medium-grade metamorphic rocks: one type (e.g., Yardoi, Kangmar, Kampa, Mabja and Malashan domes) was developed by a dominantly N-S-oriented shortening and local extension regime, whereas the other type (e.g., Ranbaand, Leo Pargil, and Gurla Mandhata domes) appears to be related to E-W extension and is always accompanied by approximately N-S-trending regional grabens and N-S-trending normal faults (Fu et al., 2017). The NHGD is representative of unevenly spaced gneiss-dome systems that may result from fault development,

---

superposition of multiple folding events, or laterally inhomogeneous properties of rocks comprising the gneiss-dome systems (Yin, 2004). Furthermore, the NHGD is one of the Himalayan leucogranite belts that resulted from anatexis (that is, crustal melting) in the Himalayan orogenic belt – with the hydrated and dehydrated melting of muscovite and biotite being the main mechanism of anataxis; the other Himalayan leucogranite belt is distributed in the Greater Himalaya Sequence (GHS) south of the Southern Tibetan Detachment GHS (STDS) (Lin et al., 2020).

Yin (2004) showed that gneiss domes are often generated by the superposition of several dome-forming mechanisms. Beaumont et al. (2004) reported that gneiss domes may be triggered by a change in crustal channel flow, such as an upward deflection or channel contraction, that causes extension of the upper crust in the Himalayan-Tibetan orogen. Lee et al. (2006, 2007) and Langille et al. (2010) also indicated a relationship between partial melting of orogenic mid-crust and channel flow processes. Although Mitsuishi et al. (2012) indicated that mid-crustal N-S extension (at relatively deep levels) and upper crustal *E*-W extension (at shallower levels) may simultaneously occur (e.g., in the Kung Co area) – which may result from the southward flow of Tibetan crust with a divergent radial component – their results do not support the idea that the overlying upper crust can be treated as a rigid upper lid of the channel flow (cf. Beaumont et al., 2004). Other studies have been carried out to investigate the conditions and timing of metamorphism, partial melting, and the relationship with Cenozoic leucogranite in the gneiss domes of the NHGD, and the relationship with N-S-trending

normal rifts, which have great implications on channel flow and/or tectonic exhumation (e.g., King et al., 2011; Zeng et al., 2011; Groppo et al., 2012; Liu et al., 2014; Cottle et al., 2015; Zhang et al., 2018; Ding et al., 2019; Yu et al., 2020; Chen et al., 2022; Xue et al., 2022). Additionally, Li et al. (2021) reported that a series of shear zones at depths of 10–15 km and two high-velocity bodies at depths of 3 km are located beneath Kangmar Gneiss Dome. These may represent eclogitic-facies rocks or mafic intrusions respectively, and provide clear geophysical evidence for the doming of upper-crustal rocks controlled by thrust stacking of middle crustal rocks. However, the relationship of the crustal migration of materials, north-south-trending rifts, and gneiss domes remains largely unexplored. In this work, we attempt to explore this relationship by generating new electrical resistivity models compiled with old electrical resistivity models and examining them with geological data and geochemical results in the region. Therefore, open questions about the region, such as the unknown southward extent of a mid-crustal channel (King et al., 2007) or whether the gneiss domes contained cooled channel flow material (King et al., 2007), can be potentially addressed with this study. Additionally, it is worth noting that previous electrical models of regions that have gneiss domes, including Turkey (Tank et al., 2018) and the Pamirs (Sass et al., 2014), have shown that those gneiss domes are located above upper-crustal resistive zones, which is thought to be related to the metamorphism associated with the active continental subduction/delamination or crustal thickening and migmatization.

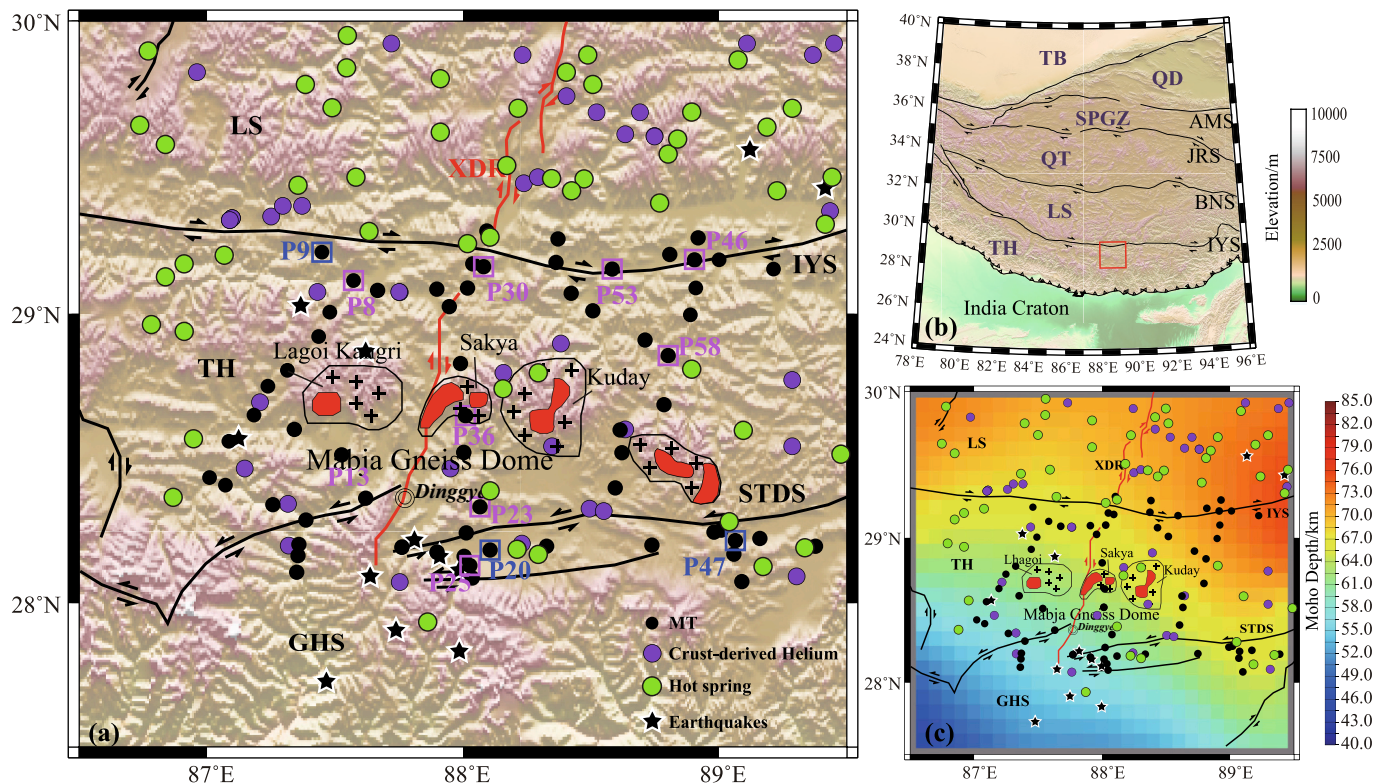The Dinggye region is located in the central part of the Tethys-

Fig. 1. Map of the study area in the vicinity of the Dinggye region, Central Himalaya. (a) Map showing the locations of MT measurement sites (black dots) used in the study. Also shown are major tectonic structures (faults and sutures in black, rifts in red; from Bian et al., 2020, and Wang et al., 2017), crustal helium (purple dots; Hou and Li, 2004; Klemperer et al., 2022), intermediate-depth earthquakes at 65–100 km depth (stars; Klemperer et al., 2022), hot springs (green dots; Klemperer et al., 2022),and the areas Lhagoi, Sakya, and Kuday that belong to the Mabja Gneiss Dome (areas marked with cross symbols and red (leucogranite core); Langille et al., 2010; Xue et al., 2022). Pink rectangles are the selected MT stations in Fig. 3. Blue rectangles are the selected MT stations in Fig. S2. (b) Regional map of the Tibetan Plateau and surroundings showing tectonic features. The red rectangle outlines the study area. (c) Map of the Moho depth in the survey area determined with seismic measurements (Li et al., 2013). XDR: Xainza-Dinggye Rift; GHS: Greater Himalaya Sequence; STDS: Southern Tibetan Detachment System; TH: Tethys–Himalaya; LS: Lhasa terrane; QT: Qiangtang terrane; IYS: Indus–Yarlung Zangbo suture; BNS: Banggong–Nujiang suture; JRS: Jinsha River suture; AMS: Animaqing suture; SPGZ: Songpan–Ganzi basin; QD: Qaidam basin; TB: Tarim basin. (For interpretation of the references to colour in this figure legend, the reader is referred to the web version of this article.)

Himalaya terrane. The southern segment of the Xainza-Dinggye rift (XDR) and the Mabja Gneiss Dome are distributed in this region (Fig. 1). The magnetotelluric (MT) method is a passive geophysical method that explores the subsurface electrical structure by measuring the time variation of electromagnetic fields at the Earth's surface. The presence of melts and/or fluids can be a potential explanation for conductive (that

is, low-resistivity) features detected in the subsurface (in addition to other materials like graphite or sulphide metals), which can result in the formation of local weak zones and contribute to possible material migration. In this study, the MT array data distributed in the Dinggye region of the Tethys-Himalaya terrane were processed, analyzed, and modelled to obtain a three-dimensional model of the lithospheric
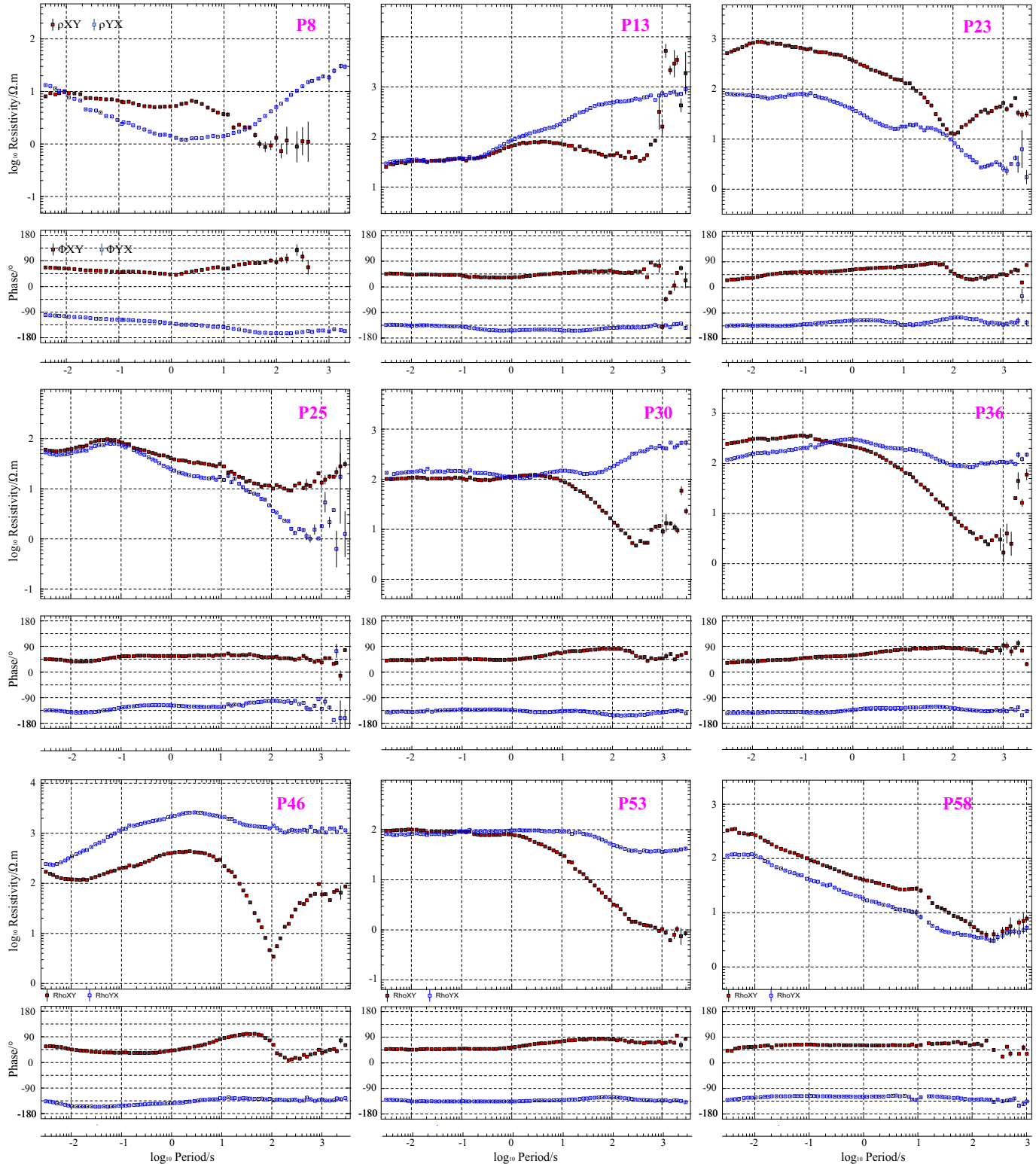

Fig. 2. Example magnetotelluric data from this study, presented as apparent resistivity and phase against period (impedance components xy and yx). See Fig. 1 for locations (Pink circles). (For interpretation of the references to colour in this figure legend, the reader is referred to the web version of this article.)

electrical structure. We then combined these models with electrical resistivity models for the region directly to the north (Sheng et al., 2021), and we compared with other electrical resistivity models for regions located directly to the east (Wei et al., 2001; Sheng et al., 2020; Xue et al., 2022). The electrical models are interpreted with the help of additional information from geological and geochemical studies. This study investigates the relationship between the electrical structure observed and the evolution of the NHGD and its influence on the N-S-trending normal fault, and further hypothesizes the formation mechanism of the XDR in the Dinggye region. In this way, the study attempts to provide insights on the mechanism of E–W extension in the Himalayan orogenic belt.

2. Data and method

2.1. Data collection and data analysis

The MT method uses measurements of the time-varying electric and magnetic fields at the surface of the Earth at selected locations or measurements stations in order to explore the subsurface electrical structure. A data set consisting of 62 MT measurements is used in this study (see Fig. 1 for the MT site location). This data set consists of new data and of data used in previous studies (for example, 18 sites along the IYS in the northern part overlap with the southern part of the region modelled by Sheng et al., 2021, and originally presented in Dong and Li,
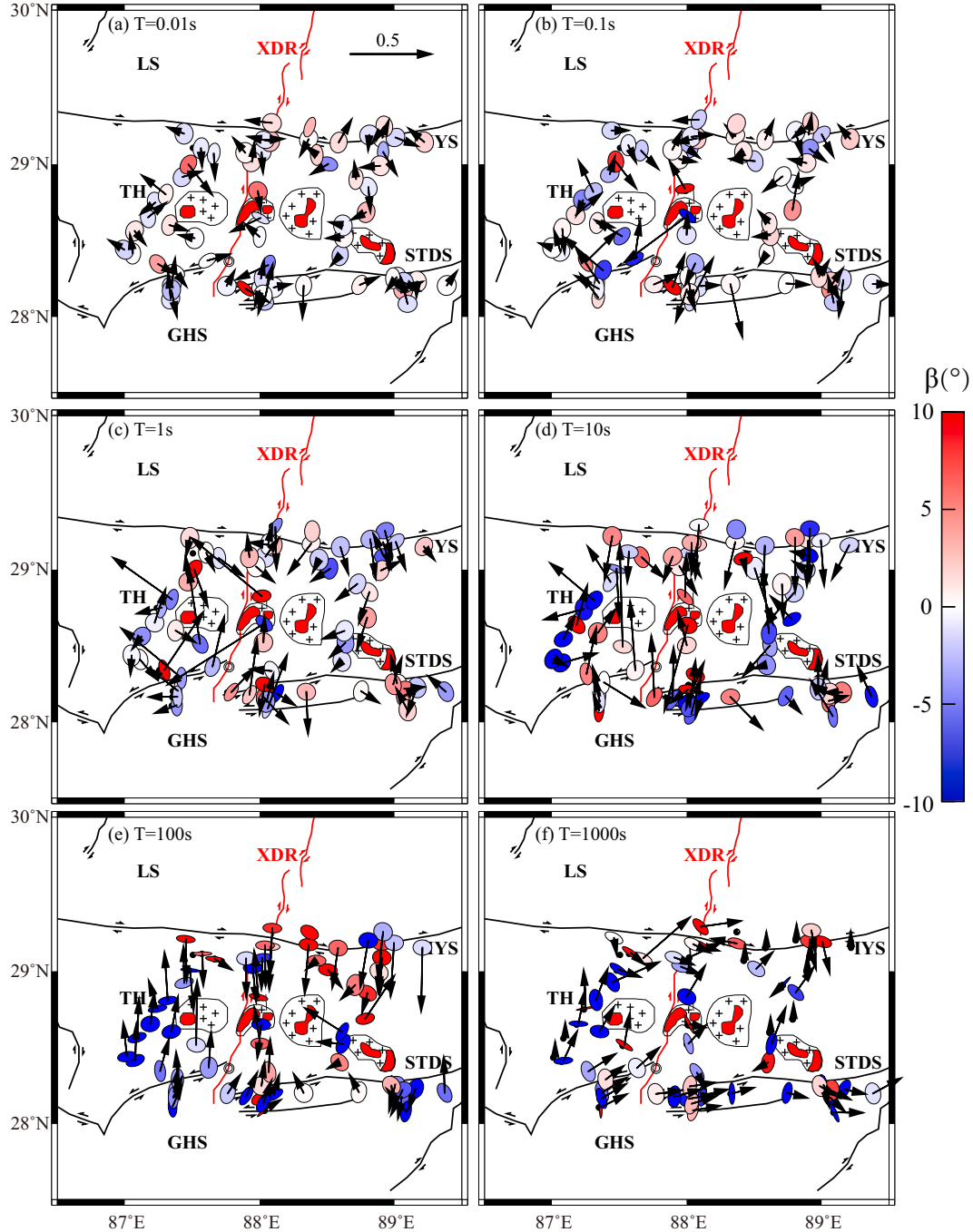

Fig. 3. Maps of real geomagnetic induction vectors (black arrows) and magnetotelluric phase tensors (ellipses). Periods of (a)-(f) 0.01 s, 0.1 s, 1 s, 10 s, 100 s, and 1000 s, respectively. Arrows point to conductors (i.e., based on the Parkinson criterion; scale arrow is in (a)). Phase tensors are colored with their phase tensor skew values (β, °). See Fig. 1 for labels.

2009).

The data were collected with Phoenix MTU-5 instruments. Electric fields were measured along perpendicular dipoles (oriented in the north-south and east-west directions) with porous-pot electrodes, and the magnetic fields were measured in three perpendicular directions (north, south, and down) with induction coils. Thus, all measurement locations recorded five components of the time-varying electromagnetic field (Ex, Ey, Hx, Hy, Hz). Typically, measurements were carried out for >20 h. This allowed a suitable period range of 0.003–3000 s to be recorded, given the optimal conditions of the study region. Frequency-dependent transfer functions were computed from the recorded time series data. Data were processed with the statistically robust algorithm of Egbert (1997) with software from Phoenix Canada, and noise was reduced at all measurement locations by employing the remote reference method (Gamble et al., 1979; Varentsov et al., 2003), from different combinations of synchronous sites. The MT data are high quality and have a low noise level (see Fig. 2 for data and Fig. 1s for locations). On the whole, the resistivity decreases with the increase of period in the beginning, which represents the presence of upper-crustal conductive zones; the resistivity increases slightly at the longest periods, which indicates that a resistive zone may be underneath these conductive zones.

The phase tensor, which is not affected by galvanic distortion effects, is used to evaluate the dimensionality of the MT data (see Caldwell et al., 2004; Booker, 2014). The skew angle β, derived from the phase tensors, can be used to decide whether a two-dimensional (2-D) Earth is a reasonable assumption or if a three-dimensional (3-D) model is required. The results from this analysis show that the phase tensor skew angles of most of the MT data are less than absolute 5° (light colors in Fig. 3) for periods <1 s, whereas the phase tensor skew angles are mainly more than absolute 5° (dark colors in Fig. 3) for periods >1 s - which indicates three-dimensional features (Fig. 3). The real part of the induction arrows, which are derived from the vertical to horizontal magnetic field transfer functions, point to the direction of increasing conductance (Parkinson, 1959). In the period range 0.01 s to 0.1 s, the orientation of the induction arrows is multi-directional (Fig. 3 a, b). In the period range 1 s to 100 s, the induction arrows point towards the center, to the Mabja Gneiss Dome (Fig. 3 c-e). For the period of 1000 s, the induction arrows point parallel to the IYS and STDS (Fig. 3f). The analysis shows that a 3-D model may better represent the collected data.

2.2. Three-dimensional (3-D) inversion

The MT data are used to generate a 3-D electrical model using the ModEM inversion algorithm (Egbert and Kelbert, 2012; Kelbert et al., 2014). According to the geometric mean of the diagonal component of the MT data (Fig. S1), the starting model is a uniform 100 Ω·m half space (although several were tested, see S.M.) and a mesh was constructed with rectilinear cells with the number of cells as follows: 60 cells in the north-south direction, 87 cells in the east-west direction, and 69 cells in the vertical direction (in addition to 7 air layers). The mesh grid has a constant cell size of 4 km in the horizontal direction in the core region and increases with a factor of 1.5 in the padding region (ten padding cells in each direction). The thickness of the first layer is 100 m in the vertical direction and increases by a factor of 1.1 in the core region and 1.5 in the padding region. The 3-D inversion uses the impedance tensor data (four complex components) and tipper data (two complex components). A total of 34 frequency points were used, 6 periods in each decade, logarithmically spaced between 0.01 s and 3000 s. Error floors were set to 5% of the sqrt (|Zxy *Zyx|) for Zxy and Zyx components and 10% of the sqrt (|Zxy *Zyx|) for the Zxx and Zyy components of the impedance tensor. An error of 5% on impedance is equivalent to about 10% for the apparent resistivity and 2.86° for the phase. Absolute error floors for the tipper data were set to 0.05 for Tx and Ty components. The smoothing parameters in the horizontal and vertical directions were the same, with the covariance chosen to be a constant value of 0.3. The starting lambda value was chosen to be 1000. The normalized root-mean-square (nR.M.S.) misfit of the inversion model was reduced from a starting value of 22.33 to 1.85 after 132 iterations. For comparison, Fig. S2 shows the horizontal slices of the electrical structure at different depths using the starting model of a 50 Ω-m half-space.

The site-by-site nR.M.S. distribution of each separate 3-D inversion is shown in Fig. 4 i. The nR.M.S. values of the majority of MT measurements are <2. Only one site exhibits a nR.M.S. fit larger than 3 (Fig. 4 i). A careful comparison of the input data and the output model responses was undertaken. Fig. S3 shows the total impedance and tipper misfit of the preferred inverse model to the observational data for some selected MT stations. Fig. S4 displays observed data and model responses at four periods; comparisons of the other periods show very similar results. The comparison between the observed data and the model response shows that they are in good agreement for periods of <100 s. However, several MT sites have notable differences in the impedance phase. The results show that the apparent resistivity is also well fit for the long period (e.g., 650 s) data, whereas the impedance phase fit appears to be somewhat inconsistent for parts of the dataset.

We observe a conductor, labelled C1, located east of the XDR at depths of 10–40 km, with its southern part at depths of approximately 10 km, close to the STDS. Conductors C3 and C4 are distributed along the IYS (Figs. 4, 5, 6). The bottom of conductor C4 appears to be at a greater depth, compared to the bottom interface of conductor C3 (Figs. 4, 5, 6). For conductors C1, C2, C3, and C4, sensitivity tests are carried out to help assess whether the observed resistive structure beneath these conductors is a robust result and required by the MT data or whether they are artificial structures produced by the inversion algorithm that lacked constraints, for example due to the limited amount of very long period data. We take the strategy of extending those features to greater depths, for example from 20 km to 40 km or to 60 km, as compared to that observed in the original model, by adding a conductive block of 1 Ω.m. The changes in the model are assessed by examining the change in nR.M.S. (as well as by analyzing the fit of the model curve to the data curve) for all sites, and especially those above or near the corresponding conductors. Sensitivity tests indicate that the conductors C1, C2, C3, and C4 are likely constrained to the bottom area of the upper crust and do not extend deeper (Fig. S5-S10), giving reliability to the large-scale resistive zone R1 underlying beneath these three conductors, which also corresponds with the resistivity variability with depth observed in the resistivity curves (as seen in Fig. 2).

Combined with the result of Sheng et al. (2021), who generated an electrical resistivity model for a region to the north of the present study area that slightly overlaps along the IYS, an obvious lithospheric resistive layer extends to the IYS west of the XDR. In contrast, the resistive layer is unobvious and discontinuous towards the east of the XDR (near the longitude of 89°E). But in this study, the resistive feature near the longitude of 89°E is more obvious than that in the previous study (Sheng et al., 2021). A possible reason may be the inclusion of tipper data in the present study and their influence on the edges of the features. Comparing the two studies, conductor C3 corresponds with conductor WC1 (Fig. 4c and Fig. 4e) and conductor C4 represents the extension of conductor EC1 in the Tethys-Himalaya terrane (Fig. 4d and Fig. 4f).

Furthermore, the identified conductive zones correspond well with low-velocity zones detected at a depth of ~30 km (Huang et al., 2020). However, the discontinuous distribution of these conductive zones is different from the continuous and widespread distribution of the low-velocity zones (although we caution that this may be due to differences in lateral resolution between the two geophysical techniques and modelling approaches (see e.g., Unsworth et al., 2023), and/or to the denser distribution of MT measurements in this local area). The high resistivity zones beneath the conductive zones in the Tethys-Himalaya terrane are consistent with the gradual increase of velocity below a depth of ~30 km (Huang et al., 2020).
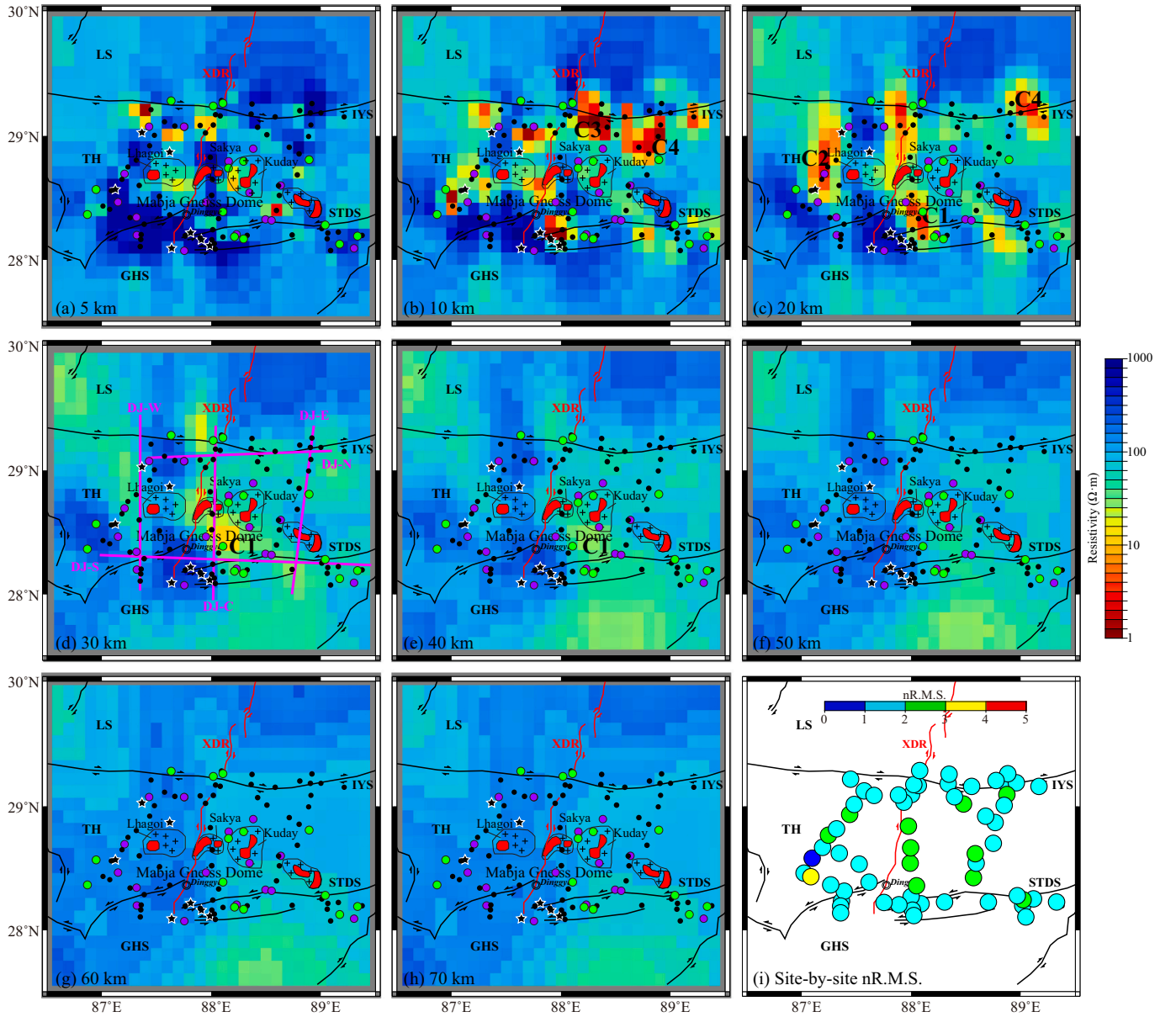
Fig. 4. Horizontal slices of the 3-D electrical resistivity model. (a) – (h) Depths of 5, 10, 20, 30, 40, 50, 60 and 70 km, respectively. C1, C2, C3 and C4 mark the conductive zones. (i) The site–by–site nR.M.S. misfit of the 3-D inversion. See Fig. 1 for labels. The pink lines indicate the profiles. (For interpretation of the references to colour in this figure legend, the reader is referred to the web version of this article.)

3. Bulk electrical conductivity and melt volume

The MT method is better at constraining the conductance than at resolving resistivity with depth. Because conductance (*C*) is the product of the effective conductivity and the thickness, the bulk conductivity σ_{eff} is computed from:

$$C = \sigma_{eff} H \tag{1}$$

where *H* is the thickness of the layer that produces the corresponding conductance.

The maximum bulk conductivity of the conductive zones C1 and C2 is approximately 2.3 S/m and 3.1 S/m, respectively, whereas that of the conductive zones C3 and C4 are several times higher (possibly >10 S/m; Fig. 7 a). Previous studies showed that the crustal conductive zones in the southern Lhasa terrane (e.g., Tethys-Himalaya terrane) may result from partial melting and aqueous fluids (e.g., saline fluids), individually or jointly (Wei et al., 2001; Chen et al., 2018). Experimental data shows

that when the temperature is 1200 °C, dry rocks begin to melt, causing the conductivity to rise; but when aqueous fluids are included, the melting temperature can be substantially reduced, possibly to 650 °C (Yardley and Valley, 1997). Sun et al. (2013) reported that in the vicinity of Dinggye region, the temperature is >700 °C at 20 km depth and >1000 °C at 40 km depth, which could meet the condition of partial melting in the presence of aqueous fluids. Additionally, the curie isothermal is at depths of 20–25 km (Xiong et al., 2016).

Assuming that the bulk conductivity of the conductive zones observed in the model results entirely from partial melting, Archie's Law is a simple method to estimate the volume fraction required (e.g., Unsworth et al., 2005; Le Pape et al., 2015; see Glover et al., 2000). Because the resistivity of the solid matrix is generally tens of times than that of the pure melt (e.g., Jin et al., 2022), the contribution of the solid matrix to the bulk conductivity can be considered negligible. Archie's law can be written (Archie, 1942; Le Pape et al., 2015)

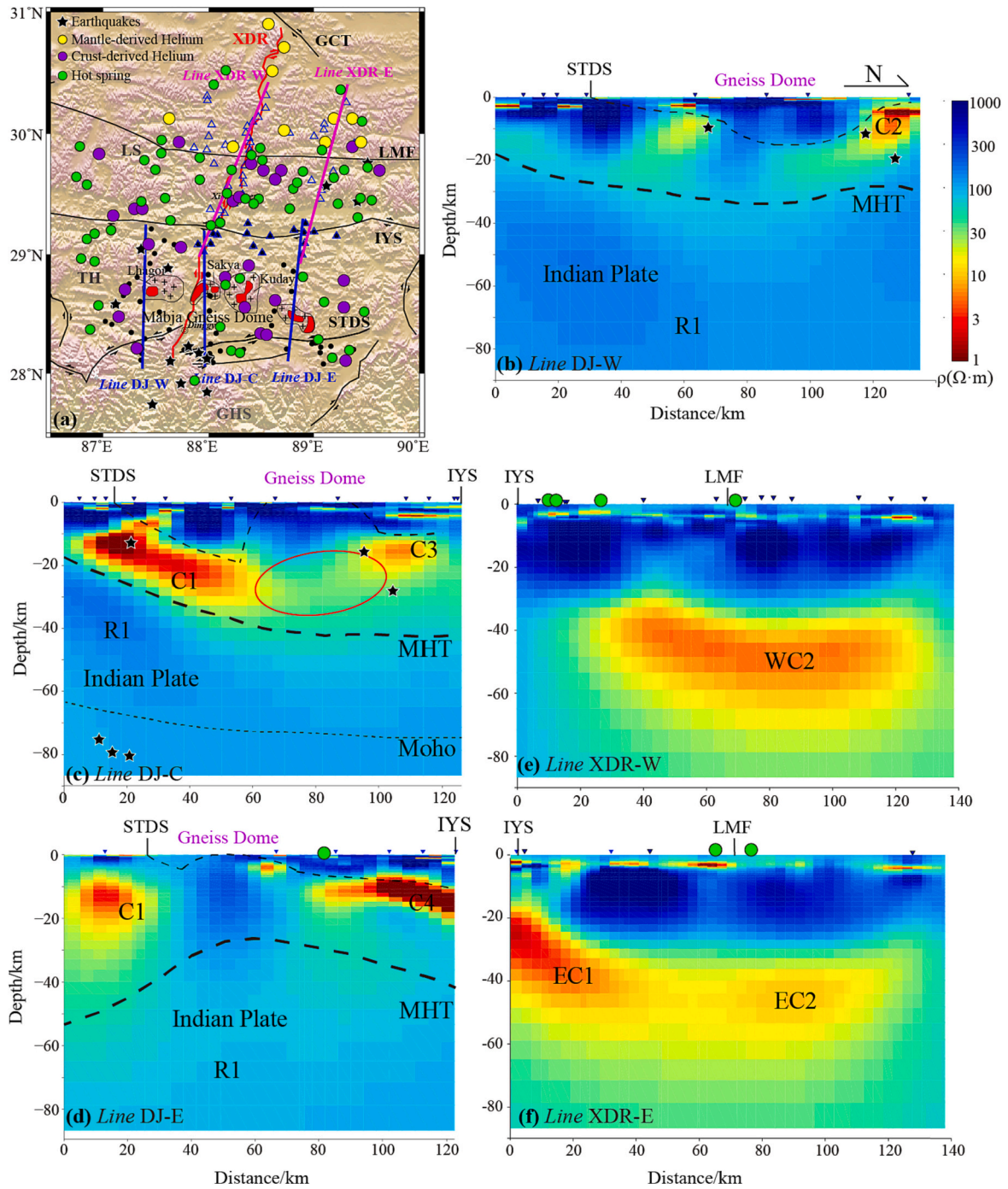$$\sigma_{eff} = C_{eff} \Phi_n \sigma_f \tag{2}$$

Fig. 5. Vertical cross sections, in the south-north direction, of the 3-D electrical resistivity models. (a) Map of the region. The locations of the south-north sections are marked. The locations of MT measurement sites used in this study are indicated with black dots and those use in Sheng et al. (2021) are indicated with blue triangles. Major tectonic structures (faults and sutures in black; rifts in red) are shown. Gneiss Domes are marked (cross symbols and red). See labels on Fig. 1. (b) Line DJ-W, (c) Line DJ-C), and (d) Line DJ-E are the sections from this study. (e) Line XDR-W and (f) Line XDR-E are sections modified from Sheng et al. (2021). MHT: Main Himalaya Thrust. The locations of the gneiss domes are indicated. A red circle marks the separation of conductor C1 and C3. Moho depth is derived from Liang et al. (2008) and Li et al. (2013). The epicenters of the intermediate-depth earthquakes are derived from Liang et al. (2008). (For interpretation of the references to colour in this figure legend, the reader is referred to the web version of this article.)

where σ_{eff} is the effective conductivity (inverse of resistivity), C_{eff} is the Archie constant, n is the Archie cementation exponent (both are empirically-derived), Φ is the volume fraction or porosity, and σ_f is the conductivity of pure melt. Previous works in the central and southern Tibetan Plateau show that the values of the constants C_{eff} and n can be taken as 1.47 and 1.30, respectively (ten Grotenhuis et al., 2005; Le Pape et al., 2015), and that the melt conductivity can be assumed to be within

the range of 1–20 S/m (e.g., Li et al., 2003).

From the minimum bulk conductivity (2.3 S/m) in these conductive zones, estimates show that when the pure melt conductivity is 20 S/m (high end of the range), at least 15% melt volume is necessary; when the pure melt conductivity is 1 S/m (low end of the range), >50% melt volume is needed (Fig. 6). Note that this is compatible with inferences for masses of melts in the mid-crust of active orogens and estimates from
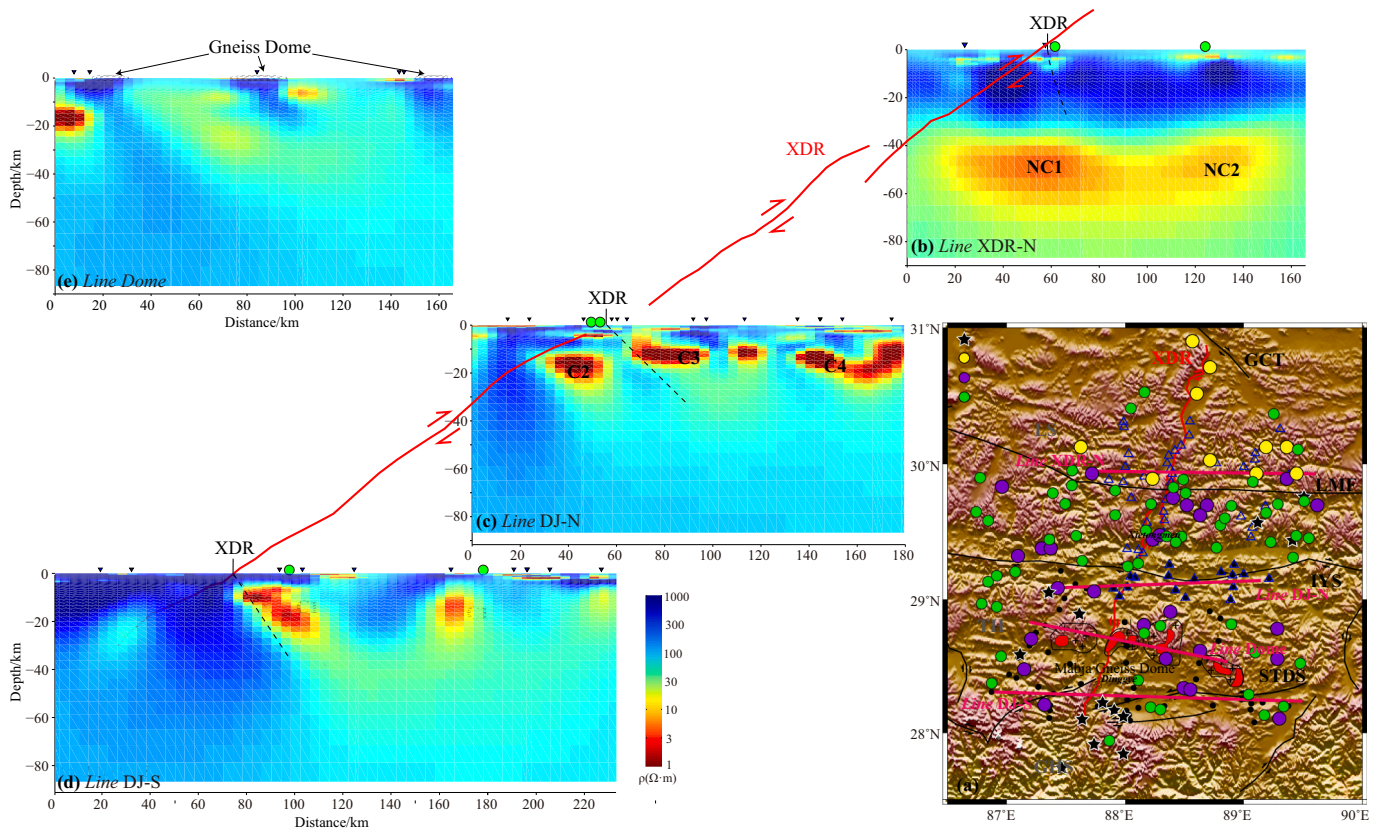
Fig. 6. Vertical cross sections, in the west-east direction, of the 3-D electrical resistivity models (a) Map of the region. The locations of the west-east sections are marked. The locations of MT measurement sites used in this study are indicated with black dots and those use in Sheng et al. (2021) are indicated with blue triangles. Major tectonic structures (faults and sutures in black; rifts in red) are shown. Gneiss Domes are marked (cross symbols and red). See labels on Fig. 1. (b) Line XDR-N is the section from Sheng et al. (2021). (c) Line DJ-N and (d) Line DJ-S are the sections from this study. (e) Another section, named Line Dome, across all the Gneiss Domes. (spatially between DJ-N and DJ-S, but offset here for clarity). Dashed lines indicate the possible inclination and extension of the XDR. LMF: Luobadui-Milashan fault; GCT: Gerecuo fault. (For interpretation of the references to colour in this figure legend, the reader is referred to the web version of this article.)
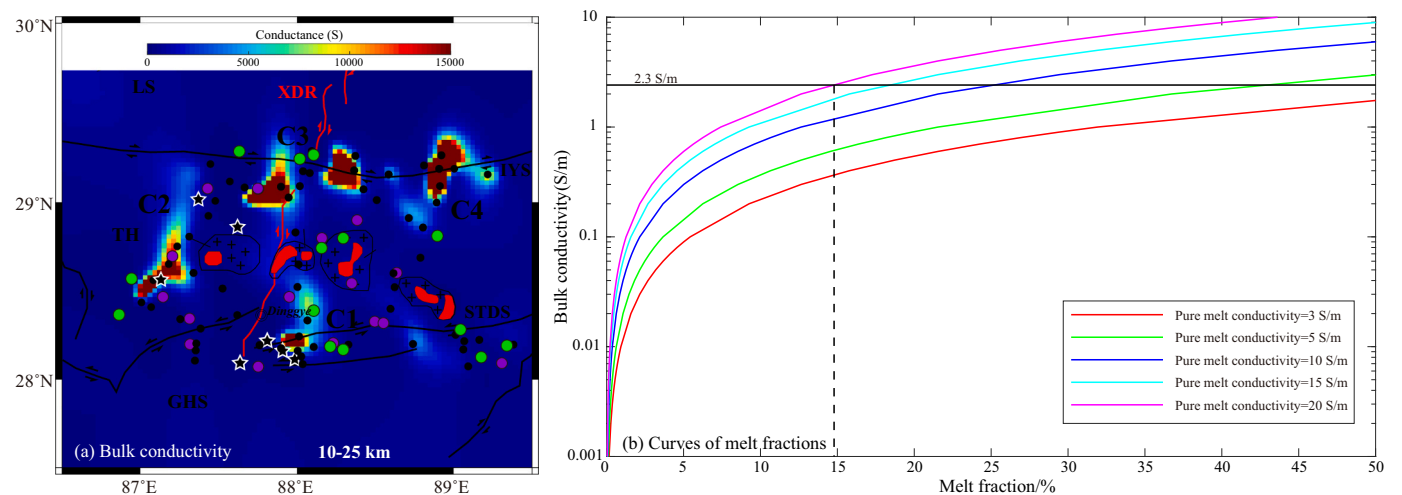

Fig. 7. a) Map of the conductance (product of conductivity and thickness) for a depth range of 10–25 km. b) Relationship between the measured bulk conductivity and the volume fraction of melt for a given pure melt conductivity (colors), which ranges 3, 5, 10, 15, and 20 S/m, computed by applying Archie's Law to a simple two-phase system. Black line marks the bulk conductivity of feature C1, which is the minimum modelled conductivity of the features C1, C2, C3 and C4.

migmatites in exhumed orogens (20–40%; Teyssier and Whitney, 2002).

The distribution of subsurface temperature shows that it is relatively high in the Dinggye region (Sun et al., 2013). Furthermore, experimental constraints suggest >6 wt% water is dissolved in Himalayan granite magmas of Oligocene-Miocene age (Hashim et al., 2013). Therefore, the

preferred interpretation is that water-rich melts contribute to the conductive zones C1 and C2 (possibly including a small amount of saline fluid). Chen et al. (2018) showed that areas with high melt fractions (e. g., >30%) reflect a crust that is either fluid-enriched or hotter in the southern Lhasa terrane. On the other hand, because the conductive

zones C3 and C4 cut across the IYS, (saline) fluids released from the subducted lithospheric plate migrate in these two zones along the subduction channel. Therefore, it is hypothesized that a larger volume of aqueous (saline) fluids may exist in conductive zones C3 and C4 than in conductive zones C1 and C2. Furthermore, enrichment with aqueous fluids may decrease the viscosity of melts, and, with the volume of melts required, the zones can meet the necessary conditions for the local flow of materials.

4. Interpretation and discussion

4.1. Subduction pattern of the Indian Plate

Previous studies hypothesized that the tearing of the downgoing Indian Plate and the decoupling of the upper crust and lithospheric mantle caused by the mid-lower crustal ductile layer contributed to the formation of the N-S-trending normal rifts (e.g., Nábělek et al., 2009; Chen et al., 2015; Li and Song, 2018; Bian et al., 2020; Sheng et al., 2021). Based on the electrical resistivity models generated in this study, in combination with models from the northern XDR (Sheng et al., 2021) and other results from the Dinggye region, we discuss the tectonic dynamic evolution of the XDR in a bigger regional context. Horizontal slices of the electrical models show that north of the IYS, the location of the XDR corresponds with conductive features in the upper crust and is located above conductive zones in the mid-lower crust (Sheng et al., 2021); in contrast, south of the IYS, the location of the XDR corresponds with conductive features in the upper and middle crust and is located above a resistive zone in the lower crust (Fig. 4). The N-S-direction cross-sections (Fig. 5) indicate that the lower crust of the Indian Plate reaches the IYS, which is broadly similar with a model for the electrical structure of the whole Lhasa terrane (Jin et al., 2022) and a deep seismic reflection survey near the Xietongmen region (45 km north of the IYS; Guo et al., 2018). The presence of ~36 Ma medium-pressure rocks in the Mabja Gneiss Dome indicates medium-pressure metamorphism at depths of 20–30 km, which likely resulted from subduction at depths of 40–60 km in the middle-lower continental crust (Ding et al., 2016). These depths are very similar to the depth range of the top surface of the resistive layer observed in the electrical models.

The detachment of the Indian crust and mantle lithosphere in the period of subduction has been proposed and discussed in several studies (e.g., Nábělek et al., 2009; Sheng et al., 2020; Bian et al., 2020). The Indian lithospheric mantle may subduct northwards, plunging deep below the Lhasa terrane, which is consistent with Miocene adakite rocks in the Xietongmen region (north of Dinggye) that are likely generated by the subduction of the Indian Plate beneath the Lhasa terrane (Chung et al., 2009). The absence of the Indian continental slab in the dacite melt source region north and south of the IYS may be taken as additional evidence that the downgoing Indian plate was characterized by deep plunging subduction and did not reach beyond the IYS in the time period between 20 and 10 Ma in this region (King et al., 2007). According to a possible average convergence rate of ~17 mm/yr along the Himalaya (Zheng et al., 2017), the Indian Plate may have moved approximately 34 km northwards since 20 Ma, which corresponds with the results above.

It has been hypothesized that subduction of the Indian Plate (including roll-back as well as tearing and break-off) resulted in upwelling of thermal materials and contributed to partial melting of the mid-lower crust (e.g., Wei et al., 2001; Unsworth et al., 2005). With the continuous northward subduction of the Indian Plate from the south and the resistance of the rigid block to the north, material adjustment beneath the Tibetan Plateau is required, which is possible in multiple directions (Mo, 2020). Previous studies have reported southern extrusion of the mid-lower crust along subduction channels (e.g., the Main Himalayan Thrust) in some regions (e.g., Sheng et al., 2021; Liu et al., 2014; Xue et al., 2022; Chen et al., 2022). The Main Himalayan Thrust (MHT; which is the tectonic boundary between the Indian lithosphere

and Tibetan crust or orogenic prism), is at a depth of approximate 47 km in the Dinggye region. In contrast, the ductile shear layer above the MHT was reported to be located at depth of approximately 22 km in the Tethys-Himalaya terrane (Guo et al., 2018), which corresponds well with the observed conductive layers. Furthermore, the conductive layers (C2/WC1 and WC2) overlying the resistor R1 were observed to be small and discontinuous in the west whereas the conductive layers (C3 and EC1) were observed to be large and continuous in the east (Fig. 4). The conductive zones C2 and C3 may result from water-rich melts (see section 3). Therefore, the conductive zones C2 and C3 (Fig. 4) may be related to southward migration of Lhasa crustal materials into the upper crust of the Tethys-Himalaya terrane, and may be due to dynamic processes that occurred at multiple time-periods. The estimated melt fractions suggest a weak rheology, which may indicate the conditions for local deformation of the overlying crust and result in the formation of an upper crustal rift.

4.2. Relationship of the electrical structure and the Northern Himalaya Gneiss Domes (NHGD)

Beneath the Mabja Gneiss Dome, a feature described as a moderately-resistive zone (Fig. 5 e) appears in the model at depths of 30–40 km (Fig. 5c). This part of the study area is a zone of low bulk conductivity and low conductance (Fig. 7a). The Mabja Gneiss Dome is mainly located at the edge of conductive zones (C2 and C3), which is a robust result because the sensitivity test shows that conductors C1 to the south and C3 to the north are not connected (Fig. S7 and S8). Interestingly, these conductive features are proposed to be related to the southern migration of crustal materials. The numerical models of Beaumont et al. (2001, 2004) show that the southward extrusion of Asian crustal materials may terminate beneath the exhumed gneiss domes or may be interrupted by them, which is incredibly consistent with the observed electrical structure – an important result.

It is reported that the multi-stage high-grade metamorphism and anatexis, which occurred from ~45 Ma to ~15 Ma during the Himalayan orogeny (King et al., 2011; Yu et al., 2011; Zhang et al., 2018), contributed to the formation of leucogranite and high-grade metamorphic rock in the Himalaya terrane (Zeng et al., 2011; Zhang et al., 2018). The presence of anatectic granites during the Oligocene-Miocene in the Mabja dome indicates southward extrusion of crustal materials (Nelson et al., 1996; Lee et al., 2006, Lee and Whitehouse, 2007; King et al., 2011), and the measured ages of dykes (12–9 Ma) constrain the time period for active southwards flow of crustal materials (King et al., 2007). However, thermochronology studies yield estimates of middle-Miocene cooling ages in the Mabja Dome (Lee et al., 2006), which may be a possible reason why a moderately-resistive zone is observed beneath the Mabja dome. That is, cooled channel flow rocks, as indicated by King et al. (2007), create conditions for a high electrical resistivity. Furthermore, isotope geochemistry results from Hou and Li (2004) suggest that hydrothermal activities since ~0.5 Ma in the Dinggye region may result from partial melting of the crust because of an asthenosphere upwelling. Therefore, conductors C2, C3, and C4, which may represent the southern extrusion of crustal material, can offer a thermal source for both the formation of leucogranite in the gneiss domes and for hydrothermal activities in the Dinggye region (Fig. 1a).

Based on the above, it could have been the case that conductors C3 and C4 were connected with conductor C1 before the middle-Miocene cooling event, in which case conductor C1 may have been related to the exhumation of the deep crustal rocks and the southern migration of crustal materials. Additionally, because Hou and Cook (2009) suggested that a cold Indian (mantle) lithosphere subducted further north and halted the heat source from the asthenosphere approximately 13–10 Ma, the radiogenic heat and tectonic (strain) heating related to the Indian Plate or thrust-nappe structure may have contributed to partial melting near the conductive zone C1, which is based on constraints from Helium isotope data reported in the Dinggye region (i.e., a crustal origin of

melts; Hou and Li, 2004; Klemperer et al., 2022). Therefore, the conductive zone C1 may be due to tectonic dynamic processes that occurred at multiple time-periods.

Conductor C1 is located at the southern endpoint of the XDR (Fig. 6), and can be explained by melt fractions of >10%. The crustal ductile layer resulted in the decoupling of the overlying brittle layer and the underlying lithosphere, leading to surface deformation (e.g., Jin et al., 2022; Sheng et al., 2021). Thus, the southern migration of crustal materials may play an important role in the formation of rifts south of the IYS (e.g., southern XDR). Combined with the results of Sheng et al. (2021), this study further indicates that upwelling of mantle-derived materials resulted from tearing of the Indian Plate and that crustal weakened zones (ductile layer) played an essential role in the formation of the XDR. According to the electrical resistivity contrast between faults and the surrounding rocks, the *E*-W-direction electrical resistivity structure beneath the XDR indicates a possible eastward inclination for the XDR (Fig. 6). Hu et al. (2016) reported that the Lagoi Kangri leucogranite is in the footwall of the XDR, which is consistent with the inclination derived from the model presented here.

Additionally, crustal shallow earthquakes located south of the IYS are concentrated at depths of approximately 20 km in the vicinity of the Dinggye region (Liang et al., 2008), which corresponds with the gradient belt between conductive zones and resistive zones. Intermediate-depth

earthquakes occur at depths of 65 to 100 km (Klemperer et al., 2022) in this region, which is below or near the Moho depth in the Tethys-Himalaya terrane (Fig. 1 c; determined with seismic measurements by Li et al., 2013). In the electrical resistivity model (Fig. 4 f, g, h), these earthquakes would be mainly located in the resistive layer at depths of >60 km, and in a mid-resistive layer in the northeast. Zhao et al. (2012) indicated that some earthquakes may be generated in the rigid resistive rock mass with conductive zones in the surroundings, which is similar with the observed electrical structure related to the shallow earthquakes, but is slightly different from the observed electrical structure at depths of >60 km. Furthermore, Liang et al. (2008) reported that earthquakes in the Dinggye region that occur at depths of 50–70 km are associated with the subducted Indian lithosphere. The fragmentary zones that resulted from the detachment of the Indian crust and mantle lithosphere in the period of subduction in the south of the IYS may be under the gravitational effect of the overlying Indian crust and could subsequently compact, which can be a possible reason for the feature of mid-high resistivity at the Moho depth (e.g., Sheng et al., 2020). Therefore, the detachment of the Indian crust and Indian lithospheric mantle may contribute to the energy of these intermedia-depth earthquakes, whereas the continuous northward subduction of the Indian lithospheric mantle could provide the material source for southern extrusion of crustal materials (e.g., represented as conductor C2 and C3),
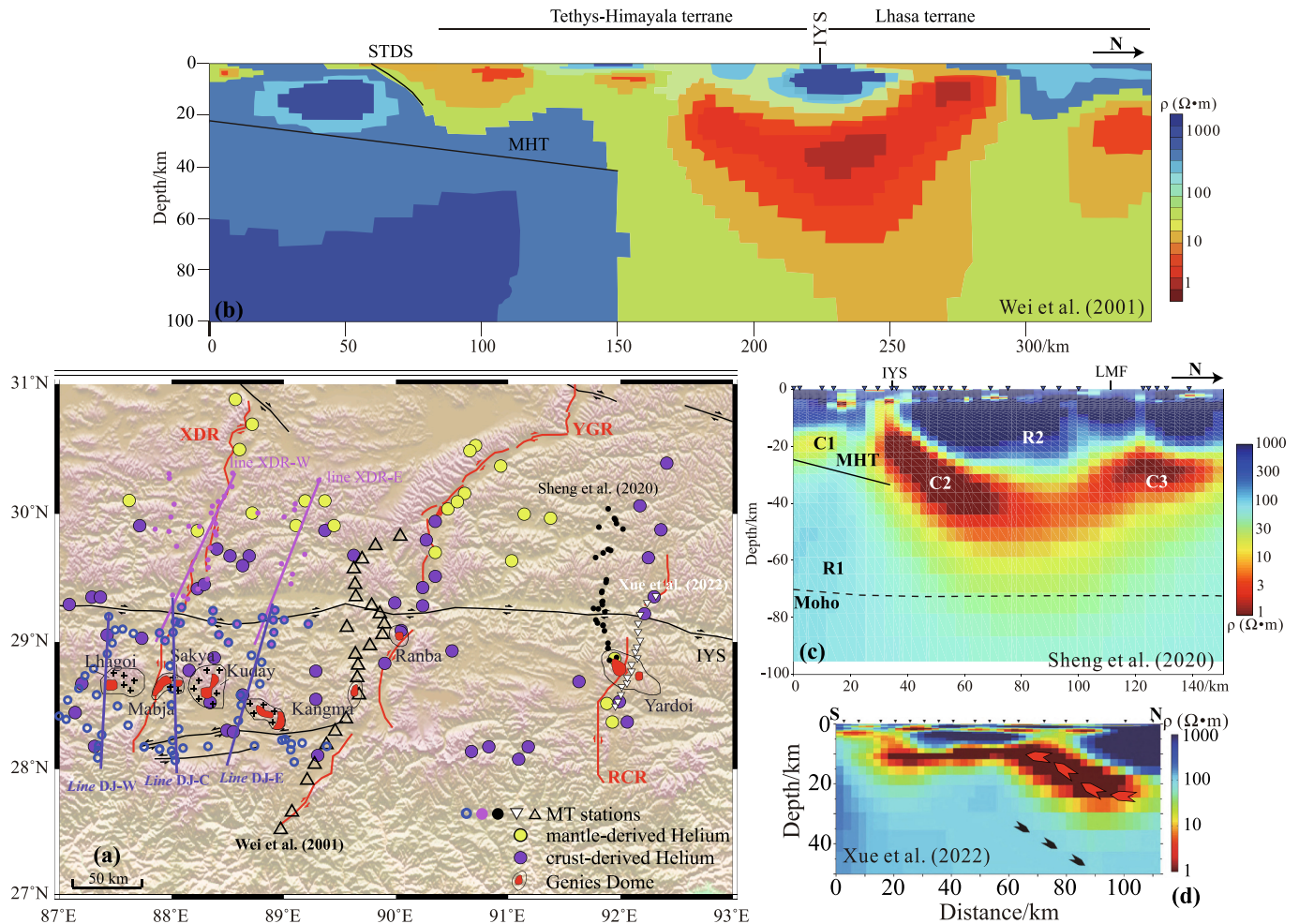

Fig. 8. Electrical resistivity models in the vicinity of the YGR and RCR. (a) Map of the region. The locations of MT measurement sites are indicated (this study, blue circles; Sheng et al., 2021, pink dots; Wei et al., 2001, black triangles; Sheng et al., 2020, black dots; Xue et al., 2022, white dots). The various rift zones are marked with red lines. Gneiss Domes across the region are marked (cross symbols and red). (b) Electrical resistivity model of Xue et al. (2022). (c) Electrical resistivity model of Sheng et al. (2020). (d) Electrical resistivity model of Wei et al. (2001). Areas Ranba, Kangma and Yardoi are Gneiss Domes in the Tethys-Himalaya terrane, east of the Mabja complex. Yadong-Gulu rift = YGR. Riduo-Cuona rift = RCR. (For interpretation of the references to colour in this figure legend, the reader is referred to the web version of this article.)

and variations in the electrical structure in the shallow area could accumulate stress prior to earthquakes.

4.3. Working hypothesis for N-S rift and gneiss dome in the Himalayas

Combined with previous studies, it seems that the relationship between the electrical resistivity structure, gneiss domes, and geothermal gas in the Mabja Gneiss Dome of the Dinggye region is similar with that in the Ranba Gneiss Dome (at a longitude of approximately 90°E) of the Yadong region (Wei et al., 2001; see Fig. 8; e.g., discontinuous conductive layers; see also Xie et al., 2017), and is different from that in the Yardoi Gneiss Dome (at a longitude of approximately 92°E) of the Cuona region (Fig. 8; e.g., continuous conductive layers). Uplifting and cooling of the Ranba and Yardoi Gneiss Domes occurred ~8–7 Ma (Chen et al., 2022) and ~ 13–10 Ma (Ding et al., 2019), respectively. Furthermore, results from Helium isotope ratio measurements in the Yadong region indicate only a crustal origin, whereas results from Helium isotope ratio measurements in the Cuona region indicate a crustal and mantle origin (Hou and Li, 2004; Klemperer et al., 2022).

Based on the observations noted above, a) it appears that where an electrically conductive layer is terminated or interrupted by a gneiss dome (for example near Mabja and Ranba) the Helium isotope ratios indicate that the geothermal gas is derived from crustal sources, which indicates that materials extruding southwards were derived from crustal partial melting; and b) it appears that where a large-scale electrically conductive layer passes across a gneiss dome (for example near Yardoi) the Helium isotope ratios indicate that the geothermal gas is derived from crustal and mantle sources, which indicates that materials extruding southwards were derived, in part, from mantle-derived materials.

Bian et al. (2020) proposed that gradual continental slab breakoff (from west to east) is linked to the evolution of the eastward-younging rifts (N-S-trending normal faults) in the Tibetan Plateau. Based on this, the subduction angle of the Indian Plate would steepen eastwards and the subduction frontier would move southwards (see also Chen et al., 2015). The observed electrical structure in the vicinity of the Dinggye region does show a lateral variation in the E-W direction. The distance to the resistive layer in the mid-lower crust, possibly representative of the subducted Indian Plate, from the IYS is various but is not monotonic. Furthermore, the northern boundary of the resistive layer from the XDR (near longitude 88°E) to the RCR (near longitude 92°E) is imaged at depths of 30–50 km (mid-lower crust) and shows no obvious difference in its distance to the IYS (Fig. 8; e.g., Sheng et al., 2020; Wei et al., 2001; Xue et al., 2022). The preceding observations indicate the similarity of the subduction frontier of the Indian crust between the longitudes of 87°E and 93°E, and also illustrate the complex topography of the descending Indian plate.

Additionally, near the XDR and the YGR, the Indian lithospheric mantle detached from the Indian crust, and subducted far from the IYS and in different regions beneath the Lhasa terrane (e.g., Sheng et al., 2021; Wang et al., 2017), which resulted in upwelling of asthenospheric materials and partial melting of the mid-lower crust in the Lhasa terrane. The Indian Plate may resist underplating of materials beneath the plate, but its frontier can facilitate the upwelling of mantle-derived materials.
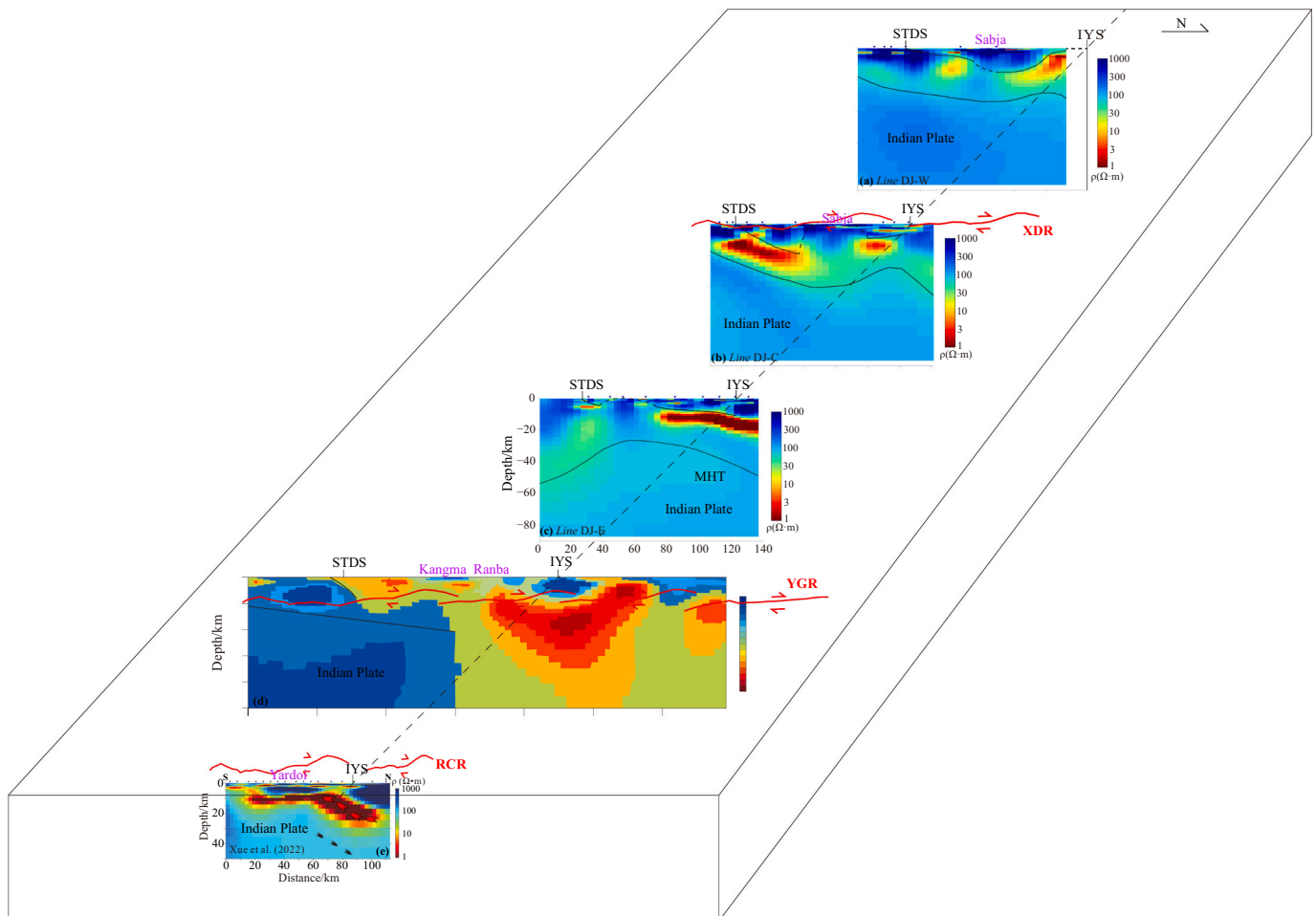

Fig. 9. Electrical resistivity models from the XDR in the west to the RCR in the east. (a), (b) and (c) are the electrical resistivity models in this study. (d) and (e) are the previous studies in Fig. 8.

Therefore, southern migration of crustal materials alone may contribute to the discontinuous conductor overlying the resistive layer, because of the possible migration distance and thermal energy. In contrast, in the vicinity of the RCR, possibly because of large-scale roll-back, the Indian Plate is characterized by steep subduction near the IYS, which likely contributes to the continuous, large-scale conductor overlying the resistive layer by facilitating southern migration of crust-mantle material and offering abundant fluids (Fig. 9 and Fig. 10). This is a possible reason why the RCR is mainly located in the Tethys-Himalaya terrane (south of the IYS).

All in all, the conductive zones observed in the mid-lower crust in the Lhasa terrane resulted from subduction, break-off, tearing or roll-back of the Indian lithosphere, which contributed to detachment of the upper crust and mantle in the Lhasa terrane and brittle deformation of the upper crust that is linked to the evolution of the N-S-trending normal rifts. In comparison, southern migration of materials along subduction channels (e.g., MHT) played an important role in the formation of the rifts in the Tethys-Himalaya terrane (Fig. 10). The variation of the observed resistive zones characterized by the Indian crust is related to the exhumation of the continental slab, metamorphism in the Tethys-Himalaya terrane and southern extrusion of materials of the Lhasa terrane.

5. Conclusions

Using data from a magnetetolluric array in the Tethys-Himalaya terrane of the southern Tibetan Plateau, we generate a 3-D electrical resistivity model covering the Dinggye region including the southern Xainza-Dinggye rift and the Mabja Gneiss Dome. Several conductive zones and a large-scale resistive feature are distributed throughout the region. According to the subsurface temperature distribution in the Dinggye region, assuming partial melting is responsible for causing the anomalies, Archie's law is used to estimate the melt volume required to explain the conductive zones.

We combine the electrical resistivity models generated in this study with electrical resistivity models from Sheng et al. (2021) of the region immediately to the north. In addition, we also compare the electrical resistivity models of regions located to the east (Wei et al., 2001; Sheng et al., 2020; Xue et al., 2022). The electrical resistivity models are interpreted based on all available, geophysical, geological, and geochemical evidence.

The conductive zones C2, C3, and C4 potentially indicate that the southern extrusion of lithospheric materials in the Lhasa terrane is related to the location of the Indian crust, and delimited and/or interrupted by the Mabja Gneiss Dome because of uplifting and cooling of the gneiss dome during the mid-Miocene. The conductive zone C1 may be related to the metamorphism, exhumation, and anatexis that occurred in the Greater Himalaya Sequence. Radiogenic heat and tectonic (strain) heating related to the Indian Plate likely contribute to partial melting in conductive zone C1, based on a predicted lack of mantle-derived thermal energy. Additionally, the estimated volume of partial melt required to explain the conductive feature C1 is lower than that required to explain conductors C3 or C4.

The observed electrical structure (such as its variation in the east-west direction) is consistent with ideas about the location and extent of tearing of the Indian Plate beneath the Lhasa terrane, near the Xainza-Dinggye rift. The results indicate that i) the mid-lower crustal conductive layers contributed to the evolution of the north-south-trending normal faults in the Lhasa terrane, ii) that the upper-crustal conductive zones resulted from the southern migration of lithospheric materials, and iii) that migration of lithospheric material thus played an essential role in the formation of the north-south-trending normal faults in the Tethys-Himalaya terrane.

CRediT authorship contribution statement

Yue Sheng: Writing – review & editing, Writing – original draft, Visualization, Validation, Software, Funding acquisition, Data curation,
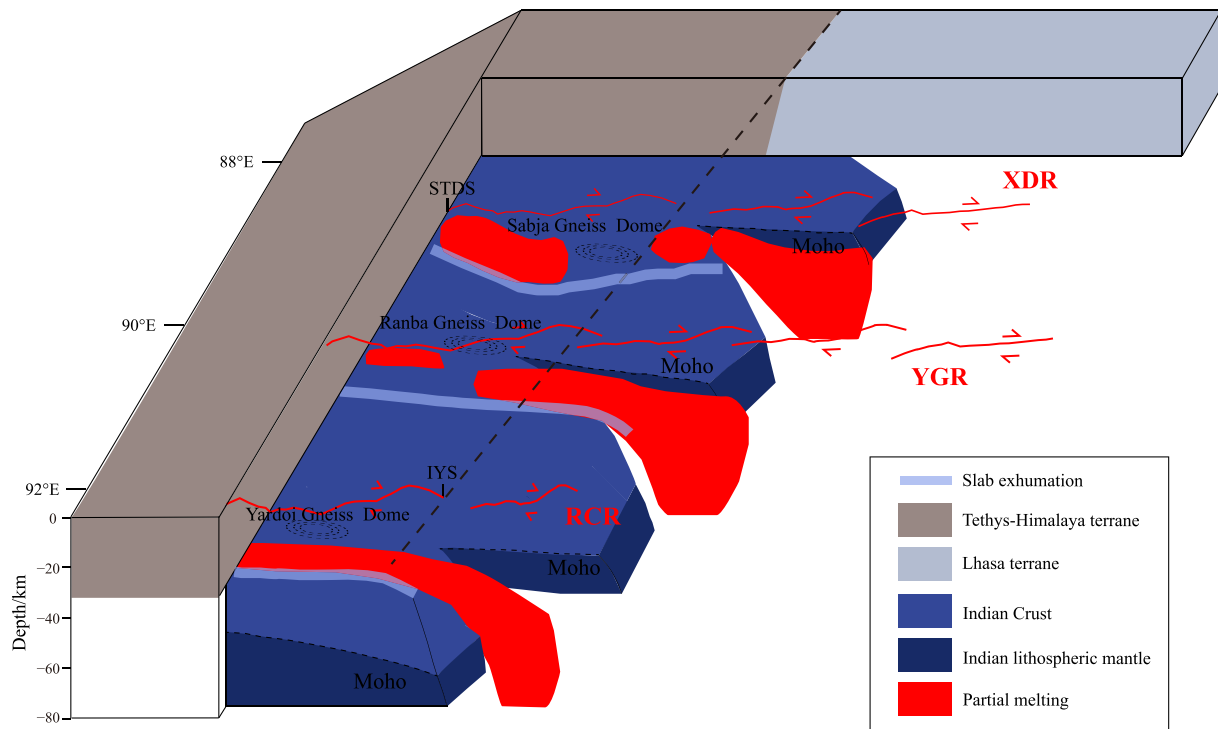

Fig. 10. Cartoon sketch of the tectonic–dynamic process in the eastern Himalayan orogenic belt. Red regions may represent material and fluid migration from the middle-lower crust to the upper crust. Black dotted circles represent the Mabja, Ranba and Yardoi gneiss domes in the Northern Himalaya Gneiss Dome belt (near longitudes of approximately 88°E, 90°E, and 92°E). White dashed lines indicate the Moho depth. (For interpretation of the references to colour in this figure legend, the reader is referred to the web version of this article.)

Declaration of Competing Interest

The authors declare that they have no known competing financial interests or personal relationships that could have appeared to influence the work reported in this paper.

Data availability

No data was used for the research described in the article.

Acknowledgements

Appendix A. Supplementary data

Supplementary data to this article can be found online at https://doi.org/10.1016/j.tecto.2023.230100.

References

Archie, G.E., 1942. The electrical resistivity log as an aid in determining some reservoir characteristics. Transactions of the American Institute of Mining, Metallurgical, and Petroleum Engineers 146, 54–62. https://doi.org/10.2118/942054-g.

Beaumont, C., Jamieson, R.A., Nguyen, M.H., Lee, B., 2001. Himalayan tectonics explained by extrusion of a low-viscosity channel coupled to focused surface denudation. Nature 414, 738–742. https://doi.org/10.1038/414738a.

Beaumont, C., Jamieson, R.A., Nguyen, M.H., Medvedev, S., 2004. Crustal channel flows: 1. Numerical models with applications to the tectonics of the Himalayan-Tibetan orogen. J. Geophys. Res. Solid Earth 109. https://doi.org/10.1029/2003JB002809.

Bian, S., Gong, J.F., Zuza, A.V., Yang, R., Tian, Y.T., et al., 2020. Late Pliocene onset of the Cona rift, eastern Himalaya, confirms eastward propagation of extension in Himalayan-Tibetan orogen. Earth Planet. Sci. Lett. 116383 https://doi.org/10.1016/j.epsl.2020.116383.

Booker, J.R., 2014. The magnetotelluric phase tensor: a critical review. Surv. Geophys. 35 (1), 7–40. https://doi.org/10.1007/s10712-013-9234-2.

Caldwell, T.G., Bibby, H.M., Brown, C., 2004. The magnetotelluric phase tensor. Geophys. J. Int. 158, 457–469. https://doi.org/10.1111/j.1365-246X.2004.02281.x.

Chen, Y., Li, W., Yuan, X., Badal, J., Teng, J., 2015. Tearing of the Indian lithospheric slab beneath southern Tibet revealed by SKS-wave splitting measurements. Earth Planet. Sci. Lett. 413, 13–24. https://doi.org/10.1016/j.epsl.2014.12.041.

Chen, J., Gaillard, F., Villaros, A., et al., 2018. Melting conditions in the modern Tibetan crust since the Miocene. Nat. Commun. 9, 1–13. https://doi.org/10.1038/s41467-018-05934-7.

Chen, S.Y., Zhang, B., Zhang, J.J., et al., 2022. Tectonic transformation from orogen-perpendicular to orogen-parallel extension in the North Himalayan Gneiss Domes: evidence from a structural, kinematic, and geochronological investigation of the Ramba gneiss dome. J. Struct. Geol. 155 https://doi.org/10.1016/j.jsg.2022.104527.

Chung, S.L., Chu, M.F., Ji, J., et al., 2009. The nature and timing of crustal thickening in southern tibet: geochemical and zircon hf isotopic constraints from postcollisional adakites. Tectonophysics 477 (1-2), 36–48. https://doi.org/10.1016/j.tecto.2009.08.008.

Cottle, J., Larson, M., Kellett, K.P., Dawn, A., 2015. How does the mid-crust accommodate deformation in large, hot collisional orogens? A review of recent research in the Himalayan orogen. J. Struct. Geol. 78, 119–133. https://doi.org/10.1016/j.jsg.2015.06.008.

Ding, H.X., Zhang, Z.M., Dong, X., et al., 2016. Early Eocene (c. 50 ma) collision of the Indian and Asian continents: constraints from the north Himalayan metamorphic rocks, southeastern Tibet. Earth Planet. Sci. Lett. 435, 64–73. https://doi.org/10.1016/j.epsl.2015.12.006.

Ding, H.X., Li, W.T., Jiang, Y.Y., 2019. The metamorphism and the tectonic implication of the Cuonadong dome , eastern Himalaya. Acta Petrol. Sin. 35 (2), 312–324. https://doi.org/10.18654/1000-0569/2019.02.03.

Dong, S.W., Li, T.D., 2009. SinoProbe: the exploration of the deep interior beneath the Chinese Continent. Acta Geol. Sin. 83 (7), 895–909.

Egbert, G.D., 1997. Robust multiple-station magnetotelluric data processing. Geophys. J. R. Astron. Soc. 136 (2), 475–496. https://doi.org/10.1111/j.1365-246X.1997.tb05663.x.

Egbert, G.D., Kelbert, A., 2012. Computational recipes for electromagnetic inverse problems. Geophys. J. Int. 189 (1), 251–267. https://doi.org/10.1111/j.1365-246x.2011.05347.x.

Fu, J.G., Li, G.M., Wang, G.H., et al., 2017. First field identification of the Cuonadong dome in southern Tibet: implications for EW extension of the north Himalayan gneiss dome. Int. J. Earth Sci. 106 (5), 1581–1596.

Gamble, T.D., Goubau, W.M., Clarke, J., 1979. Magnetotellurics with a remote magnetic reference. GEOPHYSICS 44 (1), 53–68.

Glover, P.W.J., Hole, M.J., Pous, J., 2000. A modified Archie's law for two conducting phases. Earth Planet. Sci. Lett. 180 (3–4), 369–383. https://doi.org/10.1016/S0012-821X(00)00168-0.

Groppo, C., Rolfo, F., Indares, A., 2012. Partial melting in the higher Himalayan crystallines of eastern Nepal: the effect of decompression and and Implications for the 'Channel Flow' Model. J. Petrol. 53 (5), 1057–1088. https://doi.org/10.1093/petrology/egs009.

Guo, X.Y., Gao, Y., Zhao, J.M., et al., 2018. Deep-seated lithospheric geometry in revealing collapse of the Tibetan plateau. Earth Sci. Rev. 185 https://doi.org/10.1016/j.earscirev.2018.07.013. S0012825218301594.

Hashim, L., Gaillard, F., Champallier, R., et al., 2013. Experimental assessment of the relationships between electrical resistivity, crustal melting and strain localization beneath the Himalayan-Tibetan Belt. Earth Planet. Sci. Lett. 373, 20–30. https://doi.org/10.1016/j.epsl.2013.04.026.

Hou, Z.Q., Cook, N.J., 2009. Metallogenesis of the Tibetan collisional orogen: a review and introduction to the special issue. Ore Geol. Rev. 36 (1–3), 2–24. https://doi.org/10.1016/j.oregeorev.2009.05.001.

Hou, Z.Q., Li, Z.Q., 2004. Possible location for underthrusting front of the Indus Continent: constraints from helium isotope of the geothermal gas in southern Tibet and eastern Tibet. Acta Geol. Sin. 78 (4), 482–493.

Hu, G.Y., Zeng, L.S., Chen, H., Gao, L., 2016. Assembling mechanism for the late-Miocene Mabja leucogranite pluton, Himalayan orogen. Acta Geol. Sin. 90 (8), 1737–1754.

Huang, S., Yao, H., Lu, Z., et al., 2020. High-resolution 3-D shear wave velocity model of the Tibetan Plateau: implications for crustal deformation and porphyry Cu deposit formation. J. Geophys. Res. Solid Earth 125. https://doi.org/10.1029/2019JB019215 e2019JB019215.

Jin, S., Sheng, Y., Comeau, M.J., et al., 2022. Relationship of the crustal structure, rheology, and tectonic dynamics beneath the Lhasa-Gangdese terrane (southern Tibet) based on a 3-D electrical model. J. Geophys. Res. Solid Earth 127. https://doi.org/10.1029/2022JB024318 e2022JB024318.

Kelbert, A., Meqbel, N., Egbert, G.D., Tandon, K., 2014. ModEM: a modular system for inversion of electromagnetic geophysical data. Comput. Geosci. 66, 40–53. https://doi.org/10.1016/j.cageo.2014.01.010.

King, J., Harris, N., Argles, T., et al., 2007. First field evidence of southward ductile flow of Asian crust beneath southern Tibet. Geology 35, 727–730. https://doi.org/10.1130/G23630A.1.

King, J., Harris, N., Argles, T., et al., 2011. Contribution of crustal anatexis to the tectonic evolution of India crust beneath southern Tibet. Geol. Soc. Am. Bull. 123, 218–239. https://doi.org/10.1130/B30085.1.

Klemperer, S.L., Zhao, P., Whyte, C.J., et al., 2022. Limited underthrusting of India below Tibet: He/4He analysis of thermal springs locates the mantle suture in continental collision. Proc. Natl. Acad. Sci. U. S. A. 119 (12), 1–7. https://doi.org/10.1073/pnas.2113877119.

Langille, J., Lee, F., Hacker, B., Seward, G., 2010. Middle crustal ductile deformation patterns in southern Tibet: Insights from vorticity studies in Mabja Dome. J. Struct. Geol. 32 (1), 70–85. https://doi.org/10.1016/j.jsg.2009.08.009.

Le Pape, F., Jones, A.G., Unsworth, M.J., et al., 2015. Constraints on the evolution of crustal flow beneath northern Tibet. Geochem. Geophys. Geosyst. 16 (12), 4237–4260. https://doi.org/10.1002/2015GC005828.

Lee, J., Whitehouse, M.J., 2007. Onset of mid-crustal extensional flow in southern Tibet: evidence from U/Pb zircon ages. Geology 35 (1), 45–48. https://doi.org/10.1130/G22842A.1.

Lee, J., McClelland, L., Wang, Y., et al., 2006. Oligocene–Miocene middle crustal flow in southern Tibet: geochronology of Mabja Dome. Geol. Soc. Lond. Spec. Publ. 268, 445–469. https://doi.org/10.1144/GSL.SP.2006.268.01.21.

Li, J.T., Song, X.D., 2018. Tearing of Indian mantle lithosphere from high-resolution seismic images and its implications for lithosphere coupling in southern Tibet. Proc. Natl. Acad. Sci. 115 (33), 8296–8300. https://doi.org/10.1073/pnas.1717258115.

Li, S.H., Unsworth, M.J., Booker, J.R., et al., 2003. Partial melt or aqueous fluid in the mid-crust of southern Tibet? Constraints from INDEPTH magnetotelluric data. Geophys. J. Int. 153 (2), 289–304. https://doi.org/10.1046/j.1365-246X.2003.01850.x.

Li, Y.H., Gao, T.M., Wu, Q.J., 2013. Crustal thickness map of the Chinese mainland from teleseismic receiver functions. Tectonophysics 611. https://doi.org/10.1016/j.tecto.2013.11.019.

Li, H.Q., Gao, R., Li, W.H., Carbonell, R., et al., 2021. The Mabja dome structure in southern Tibet revealed by deep seismic reflection data and its tectonic implications. J. Geophys. Res. Solid Earth 126. https://doi.org/10.1029/2020JB020265 e2020JB020265.

Liang, X., Zhou, S., Chen G, Y.J., et al., 2008. Earthquake distribution in southern Tibet and its tectonic implications. J. Geophys. Res. 113, B12409. https://doi.org/10.1029/2007JB005101.

Lin, C., Zhang, J.J., Wang, X.Y., et al., 2020. Oligocene initiation of the South Tibetan Detachment System: Constraints from syn-tectonic leucogranites in the Kampa Dome, Northern Himalaya. Lithos 354-355. https://doi.org/10.1016/j.lithos.2019.105332.

Liu, Z.C., Wu, F.Y., Ji, W.Q., et al., 2014. Petrogenesis of the Ramba leucogranite in the Tethyan Himalaya and constraints on the channel flow model. Lithos 208-209, 118–136. https://doi.org/10.1016/j.lithos.2014.08.022.

Mitsuishi, M., Wallis, S.R., Aoya, M., et al., 2012. E–W extension at 19 Ma in the Kung co area, S. Tibet: evidence for contemporaneous e–w and n–s extension in the Himalayan orogen. Earth Planet. Sci. Lett. 325-326, 10–20. https://doi.org/10.1016/j.epsl.2011.11.013.

Mo, X.X., 2020. Growth and evolution of crust of Tibetan Plateau from perspective of magmatic rocks. Earth Sci. 45 (7), 2245–2257. https://doi.org/10.3799/dqkx.2020.160.

Nábělek, J., Hetényi, G., Vergne, J., et al., 2009. Underplating in the Himalaya-Tibet collision zone revealed by the Hi-CLIMB experiment. Science 325, 1371–1374. https://doi.org/10.1126/science.1167719.

Nelson, K.D., Zhao, W., Brown, L.D., et al., 1996. Partially Molten Middle Crust beneath Southern Tibet: Synthesis of Project INDEPTH results. Science 274 (5293), 1684–1688. https://doi.org/10.1126/science.274.5293.1684.

Parkinson, W.D., 1959. Directions of rapid geomagnetic fluctuations. Geophys. J. Roy. Astron. Soc. 2 (1), 1–14. https://doi.org/10.1111/j.1365-246X.1959.tb05776.x.

Sass, P., Ritter, O., Ratschbacher, L., et al., 2014. Resistivity structure underneath the pamir and southern tian Shan. Geophys. J. Int. 1, 564–579.

Sheng, Y., Jin, S., Lei, L.L., et al., 2020. Deep thermal state on the eastern margin of the Lhasa-Gangdese belt and its constraints on tectonic dynamics based on the 3-D electrical model. Tectonophysics 793. https://doi.org/10.1016/j.tecto.2020.228606.

Sheng, Y., Jin, S., Comeau, M.J., et al., 2021. Lithospheric structure near the northern Xainza-Dinggye Rift, Tibetan Plateau – implications for rheology and tectonic dynamics. Journal of Geophysical Research: Solid. Earth. https://doi.org/10.1029/2020JB021442.

Sun, Y.J., Dong, S.W., Zhang, H., et al., 2013. 3D rheological structure of the continental lithosphere beneath China and adjacent regions. Chin. J. Geophys. 56 (5), 546–558. https://doi.org/10.1002/cjg2.20052.

Tank, S.K.M., Özaydın, S., Karaş, M., 2018. Revealing the electrical properties of a gneiss dome using three-dimensional magnetotellurics: burial and exhumation cycles associated with faulting in central anatolia, Turkey. Phys. Earth Planet. Inter. 283.

ten Grotenhuis, S.M., Drury, M.R., Spiers, C.J., Peach, C.J., 2005. Melt distribution in olivine rocks based on electrical conductivity measurements. J. Geophys. Res. 110, 1–11. https://doi.org/10.1029/2004JB003462.

Teyssier, C., Whitney, D., L., 2002. Gneiss domes and orogeny. Geology 30 (12), 1139–1142. https://doi.org/10.1130/0091-7613(2002)030<1139:GDAO>2.0.CO;2.

Unsworth, M.J., Jones, A.G., Wei, W., et al., 2005. Crustal rheology of the Himalaya and southern Tibet inferred from magnetotelluric data. Nature 438 (7064), 78–81. https://doi.org/10.1038/nature04154.

Unsworth, M., Comeau, M.J., Diaz, D., Brasse, H., et al., 2023. Crustal structure of the Lazufre volcanic complex and the Southern Puna from 3-D inversion of magnetotelluric data: implications for surface uplift and evidence for melt storage and hydrothermal fluids. Geosphere 19, 21. https://doi.org/10.1130/GES02506.1.

Varentsov, I.M., Sokolova, E.Y., Martanus, E., Nalivaiko, K., BEAR Working Group, 2003. System of electromagnetic field transfer operators for the BEAR array of simultaneous soundings: methods and results. Izv. Phys. Solid Earth 39, 118–148.

Wang, G., Wei, W.B., Ye, G.F., 2017. 3-D electrical structure across the Yadong-Gulu rift revealed by magnetotelluric data: New insights on the extension of the upper crust and the geometry of the underthrusting Indian lithospheric slab in southern Tibet. Earth Planet. Sci. Lett. 474, 172–179. https://doi.org/10.1016/j.epsl.2017.06.027.

Wei, W., Unsworth, M., Jones, A., et al., 2001. Detection of widespread fluids in the Tibetan crust by magnetotelluric studies. Science 292 (5517), 716–719. https://doi.org/10.1126/science.1010580.

Wessel, P., Smith, W., 1998. New, improved version of Generic Mapping Tools released. Eos Trans. AGU 79, 579. https://doi.org/10.1029/98EO00426.

Xie, C.L., Jin, S., Wei, W., et al., 2017. Varying Indian crustal front in the southern Tibetan plateau as revealed by magnetotelluric data. Earth Planets & Space 69 (1), 147. https://doi.org/10.1186/s40623-017-0734-z.

Xiong, S.Q., Yang, H., Ding, Y.Y., et al., 2016. Characteristics of Chinese continent curie point isotherm. Chin. J. Geophys. 59 (10), 3604–3617. https://doi.org/10.6038/cjg20161008 (in Chinese).

Xue, S., Lu, Z.W., Li, W.H., et al., 2022. Electrical resistivity structure beneath the central Cona-Oiga rift, southern Tibet, and its implications for regional dynamics. Earth Sci. Front. 29 (2), 393–401. https://doi.org/10.13745/j.esf.sf.2022.2.3.

Yardley, B.W.D., Valley, J.W., 1997. The petrologic case for a dry lower crust. J. Geophys. Res. 102 (B6), 12173–12185. https://doi.org/10.1029/97jb00508.

Yin, A., 2004. Gneiss domes and gneiss dome systems. In: Special Paper of the Geological Society of America, 380. https://doi.org/10.1130/0-8137-2380-9.1.

Yin, A., Harrison, T.M., 2000. Geologic evolution of the Himalayan-Tibetan orogen. Annu. Rev. Earth Planet. Sci. 28, 211–280. https://doi.org/10.1146/annurev.earth.28.1.211.

Yu, J.J., Zeng, L.S., Liu, J., et al., 2011. Early Miocene leucogranites in Dinggye area, southern Tibet: Formation mechanism and tectonic implications. Acta Petrol. Sin. 27 (7), 1961–1972.

Yu, Y., Xu, X., Gao, R., Guo, X.Y., 2020. Seismic evidence for tectonic affinity of the Yungbwa ophiolitic complex, western Tibet. Chin. J. Geophys. 63 (3), 840–846. https://doi.org/10.6038/cjg2020N0220 (In Chinese).

Zeng, L.S., Gao, L.E., Xie, K.J., Jing, L.Z., 2011. Mid-Eocene high Sr/Y granites in the northern Himalayan gneiss domes: melting thickened lower continental crust. Earth Planet. Sci. Lett. 303, 3–4. https://doi.org/10.1016/j.epsl.2011.01.005.

Zhang, Z.M., Kang, D.Y., Ding, H.X., et al., 2018. Partial melting of himalayan orogen and formation mechanism of leucogranite. Earth Sci. 43 (1), 17 (Abstract in English). CNKI:SUN:DQKX.0.2018-01-007.

Zhao, G.Z., Unsworth, M.J., Zhan, Y., et al., 2012. Crustal structure and rheology of the Longmenshan and Wenchuan mw 7.9 earthquake epicentral area from magnetotelluric data. Geology 40 (12), 1139–1142. https://doi.org/10.1130/g33703.1.

Zheng, G., Wang, H., Wright, T.J., et al., 2017. Crustal deformation in the India-Eurasia collision zone from 25 years of GPS measurements. J. Geophys. Res. Solid Earth 122, 9290–9312. https://doi.org/10.1002/2017JB014465.